

See discussions, stats, and author profiles for this publication at: <https://www.researchgate.net/publication/261747156>

# Toward Deep Blue Nano Hope Diamonds: Heavily Boron-Doped Diamond Nanoparticles

ARTICLE *in* ACS NANO · APRIL 2014

Impact Factor: 12.88 · DOI: 10.1021/nn500573x · Source: PubMed

---

CITATIONS

16

READS

197

## 8 AUTHORS, INCLUDING:



Steffen Heyer

University of Wuerzburg

2 PUBLICATIONS 21 CITATIONS

[SEE PROFILE](#)



Stuart Turner

University of Antwerp

171 PUBLICATIONS 1,811 CITATIONS

[SEE PROFILE](#)



Yinggang Lu

University of Colorado Boulder

21 PUBLICATIONS 184 CITATIONS

[SEE PROFILE](#)



Jo Verbeeck

University of Antwerp

190 PUBLICATIONS 2,859 CITATIONS

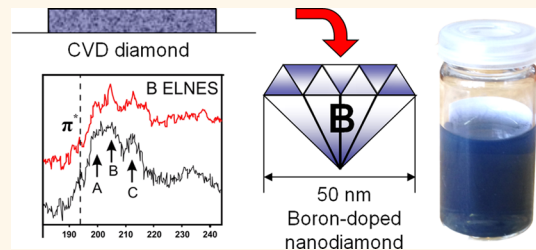
[SEE PROFILE](#)

# Toward Deep Blue Nano Hope Diamonds: Heavily Boron-Doped Diamond Nanoparticles

Steffen Heyer,<sup>†,#</sup> Wiebke Janssen,<sup>‡,§,#</sup> Stuart Turner,<sup>||,\*</sup> Ying-Gang Lu,<sup>||</sup> Weng Siang Yeap,<sup>‡,§</sup> Jo Verbeeck,<sup>||</sup> Ken Haenen,<sup>‡,§,\*</sup> and Anke Krueger<sup>†,‡,\*</sup>

<sup>†</sup>Institut für Organische Chemie, Julius-Maximilians-Universität Würzburg, Am Hubland, D-97074 Würzburg, Germany, <sup>‡</sup>IMOMEC, IMEC vzw, Wetenschapspark 1, B-3590 Diepenbeek, Belgium, <sup>§</sup>Institute for Materials Research (IMO), Hasselt University, Wetenschapspark 1, B-3590 Diepenbeek, Belgium, <sup>||</sup>EMAT, University of Antwerp, Groenenborgerlaan 171, B-2020 Antwerp, Belgium, and <sup>†</sup>Wilhelm Conrad Röntgen Research Center for Complex Material Systems (RCCM), Julius Maximilians-Universität Würzburg, Am Hubland, D-97074 Würzburg, Germany. <sup>#</sup>S. Heyer and W. Janssen contributed equally.

**ABSTRACT** The production of boron-doped diamond nanoparticles enables the application of this material for a broad range of fields, such as electrochemistry, thermal management, and fundamental superconductivity research. Here we present the production of highly boron-doped diamond nanoparticles using boron-doped CVD diamond films as a starting material. In a multistep milling process followed by purification and surface oxidation we obtained diamond nanoparticles of 10–60 nm with a boron content of approximately  $2.3 \times 10^{21} \text{ cm}^{-3}$ . Aberration-corrected HRTEM reveals the presence of defects within individual diamond grains, as well as a very thin nondiamond carbon layer at the particle surface. The boron K-edge electron energy-loss near-edge fine structure demonstrates that the B atoms are tetrahedrally embedded into the diamond lattice. The boron-doped diamond nanoparticles have been used to nucleate growth of a boron-doped diamond film by CVD that does not contain an insulating seeding layer.



**KEYWORDS:** nanodiamond · boron doping · nanoparticles · milling · CVD diamond · TEM · EELS

Boron-doped diamonds in their natural and synthetic forms (HPHT and CVD) have a wide range of possible applications. Besides their evident use as gemstones, the most famous being the Hope and the Blue Wittelsbach diamonds,<sup>1,2</sup> B-doped CVD diamond films show the widest known electric potential window, making them an ideal material to be used as electrochemical electrodes.<sup>3–5</sup> Despite years of research, interest is still growing, ranging from very fundamental investigations on its (superconducting) properties<sup>6–8</sup> to possible uses in new applications such as X-ray beam monitoring.<sup>9</sup>

To date, nanocrystalline diamond particles with homogeneous boron doping have not been reported as such. However, diamond powders coated with a boron-doped surface layer have been investigated. In these attempts the boron was present in the outer shell, but not present in the undoped diamond core, and the size of the clustered particles was relatively large.<sup>10</sup>

Further work was done in order to use these particles for catalytic applications (*i.e.*, by platinization).<sup>11</sup> Another approach was reported using diamond microcrystals obtained from CVD films as the catalyst support.<sup>12</sup> The growth of a boron-doped diamond layer on a conductive carbon material (here glassy carbon) was also reported.<sup>13</sup> But still, fully doped, well-dispersed diamond nanoparticles with small diameters are not only of fundamental interest to the scientific community; a broad range of applications can be envisaged for this type of material. The application of boron-doped seeds for the growth of homogeneous boron-doped diamond films is especially attractive. In order to understand the properties of boron-doped nanoparticles, structural features such as the location of the boron atoms in the nanocrystal, the superconducting properties, or the occurrence of charge transfer upon surface functionalization with suitable dyes need to be investigated.<sup>14</sup> Later on, there could be applications in electrochemistry

\* Address correspondence to anke.krueger@uni-wuerzburg.de, ken.haenen@uhasselt.be, and stuart.turner@ua.ac.be.

Received for review January 28, 2014 and accepted April 9, 2014.

Published online  
10.1021/nn500573x

© XXXX American Chemical Society

and atomic force microscopy (using the highly doped particles as starting material in molds to form conducting AFM tips for scanning spreading resistance measurements (SSRM)).<sup>15</sup> In general, they could be used as seeding crystals during CVD to avoid a first insulating layer between the substrate and the growing diamond films, which is undesirable for most electronic and electrochemical applications, as it increases the interface resistance between diamond layer and substrate. Therefore, it is of great interest to produce diamond nanoparticles with high boron content at the C-lattice positions in a way that can be upscaled for the above-mentioned applications.

Both natural and synthetic diamond (nano)particles are known to contain lattice defects and impurities. Several defect centers have been investigated in great detail, among them, the most prominent, the NV center, but also, for example, silicon-based defects (*i.e.*, SiV) and nickel- or chromium-related defects.<sup>16–19</sup> Numerous applications of these nanoparticles have been reported. Besides nanodiamond-based biomedical markers and sensors that rely on the stable fluorescence of lattice defects such as the NV center,<sup>16</sup> single photon sources,<sup>17</sup> nanomagnetometers,<sup>20</sup> and setups for optical applications such as STED microscopy<sup>21</sup> can be fabricated using suitably sized and structured nanodiamonds.

Methods for the production of such doped nanoparticles include the implantation of atoms or clusters into existing nanoparticles, the growth of doped crystallites by chemical vapor deposition, and top-down approaches starting from larger objects that already contain the respective lattice defects.

Ion implantation can be used to treat already available nanoparticles; however, the lattice suffers damage from the high impact of the implanted objects.<sup>22</sup> In the case of diamond such damage can result in the formation of dislocations or the partial or even complete graphitization of the nanoparticles.<sup>23</sup> Another issue is related to the location of the foreign atoms. Implantation does not guarantee that the foreign atoms are placed at lattice positions. Implantation of atoms at unwanted interstitial locations as well as the formation of defect clusters cannot be excluded. Nevertheless, this technique has been used to produce diamond nanostructures with NV centers.<sup>24</sup> In the case of boron-doping this method, however, is not applicable due to the large number of necessary defects that cannot be healed by annealing. The production of doped nanoparticles by CVD methods is limited to small amounts of material, as the process has to be stopped at a very early stage.<sup>25,26</sup> The resulting particles typically show a very broad size distribution and often irregular shape. In some cases, though, considerable control of the properties of these CVD-grown particles has been achieved.<sup>27</sup> Also the removal of the substrate can damage the obtained nanocrystallites. Furthermore,

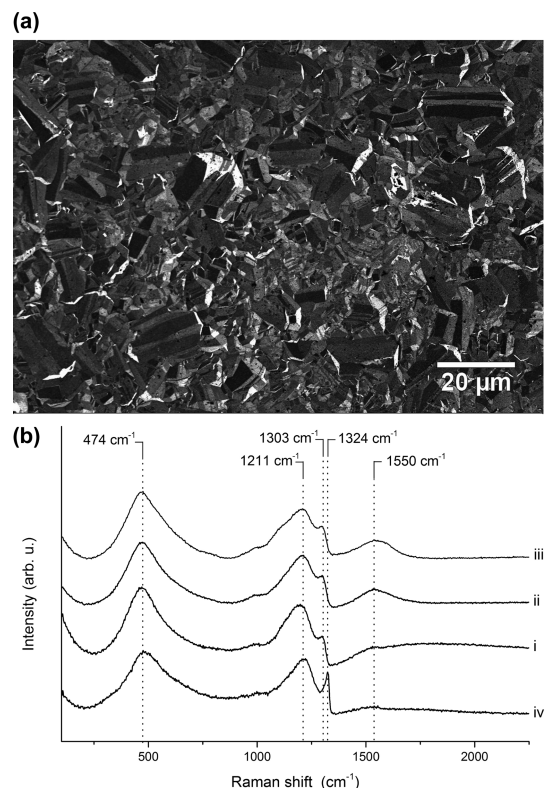


**Figure 1.** (a) SEM image of the original boron-doped film showing grain sizes in the micrometer range; (b) Raman spectra of the back side of the initial film (iv), and the three size fractions (spectra i–iii; see dynamic light scattering (DLS) results in Figure 2 for size distributions) after crushing.

this technique typically leads to overgrown particles with a defect-free core and a doped shell. This inhomogeneous distribution of defects is undesirable for most applications.<sup>10</sup>

The production of diamond nanoparticles from bulk and CVD diamond has been demonstrated by some of us for diamond containing SiV<sup>17,28</sup> or NV<sup>20</sup> color centers. The latter has also been reported for the crushing of HTHP diamond.<sup>29</sup> Such methods are typically accompanied by differing levels of sample contamination, *e.g.*, by zirconia from milling beads, and surface graphitization is observed.<sup>28</sup> Additionally, the concentration of these defects is typically orders of magnitude lower than for boron-doped materials.

Here we report on the production of truly boron-doped diamond nanoparticles, starting from highly boron-doped polycrystalline CVD diamond, leading to noncontaminated, colloidal solutions of the boron-doped ND particles.

## RESULTS AND DISCUSSION

The starting material was a 14.5 μm thick, polycrystalline, B-doped diamond film produced by microwave plasma-enhanced chemical vapor deposition (MW PE CVD). The film features randomly oriented microcrystals with an average crystal size around 7 μm, with single grains measuring up to 20 μm (Figure 1a).

Raman spectroscopy (excitation at  $\lambda = 445$  nm) reveals a clear peak at  $\sim 1325\text{ cm}^{-1}$  related to  $\text{sp}^3$ -bonded carbon (Figure 1b, spectrum (iv)). The Fano resonance as well as the band at  $1211\text{ cm}^{-1}$  confirms boron doping above  $10^{20}\text{ cm}^{-3}$ .<sup>30</sup> Nanosized grains of the early deposition, hence a high density of  $\text{sp}^2$ -containing grain boundaries, explain the presence of the G-band at  $\sim 1550\text{--}1570\text{ cm}^{-1}$  visible in the spectrum from the backside of the film (Figure 1b, (iv)).

The polycrystalline diamond film was isolated from its silicon substrate by chemical etching in a tetramethylammonium hydroxide (TMAH) solution. The absence of significant amounts of silicon from the substrate was proven by energy-dispersive X-ray spectroscopy (EDX). Further evidence was obtained by the absence of the respective signals in the Raman spectrum (Figure 1b) recorded at 445 nm excitation wavelength.

Crushing of the film was carried out using a vibration mill and grinding balls made of tempered steel. The choice of the equipment's constituting material is of importance, as a compromise between sufficient hardness and easy removal of abrasion debris has to be found. In previous reports we used zirconia-coated milling vessels as well as zirconia milling beads.<sup>31</sup> This material exhibits a very high hardness; however, diamond is still harder and hence some abrasion is observed. As nanoscale zirconia is very difficult to remove (treatment with phosphoric acid or strong base is required for a prolonged time followed by, for example, a chromatography step),<sup>32</sup> we opted for steel as a softer yet easier to remove material here. The crushing was carried out in a multistep fashion in order to avoid material heating and subsequent graphitization. After milling, a mixture of diamond powder and iron abrasion is obtained. The iron and most of the other steel components can be removed using hydrochloric acid treatment at elevated temperature. The remaining contaminants are dissolved during the oxidative treatment (see below). The resulting diamond material exhibits a black color, and Raman spectra reveal the existence of large amounts of  $\text{sp}^2$  carbon within the material (Figure S1, Supporting Information). An attempt to separate diamond nanoparticles as a colloidal solution from this initial powder by dispersing it and precipitating larger fractions failed. As can be seen in Figure S2, the obtained brown colloid did not contain diamond. Instead, disordered graphitic material was observed. The latter in part stems from the grain boundaries of the CVD diamond film (see above). Another part is formed during the milling; the high energy impact of the grinding balls and the generation of dangling bonds at the freshly generated surfaces promote the reconstruction of the particle surface to  $\text{sp}^2$  carbon. The resulting  $\text{sp}^2$  carbon nuclei lead to subsequent formation of more extended areas of graphitic material on the particle surfaces due to local

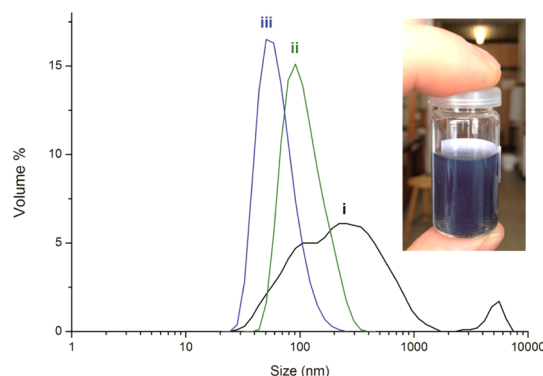


**Figure 2.** Particle size distribution of the three size fractions (i to iii) obtained by fractionated centrifugation of the diamond suspension after purification and deep blue colloidal solution of B:ND fraction iii in water (inset). Centrifugation was carried out at 5000 rpm for 5 min for ii and 8000 rpm for 5 min for iii. Colloid i contains the entire amount of the crushed diamond sample including all particle sizes.

heating in the milling mixture. Hence, an additional step for the removal of this carbonaceous material had to be conceived. As has been reported in the literature,<sup>33</sup> the reactivity of perfectly ordered carbon in the diamond lattice is lower compared to disordered  $\text{sp}^3$  carbon and any kind of graphitic material. Here, the oxidative removal of the  $\text{sp}^2$  carbon was carried out using a treatment with a hot mixture of concentrated sulfuric and nitric acid (9:1). This treatment removes not only most of the  $\text{sp}^2$  carbon but also the remaining metallic impurities such as chromium and manganese from the composition of the tempered steel milling equipment. Dispersing the resulting material yielded a deep blue colloidal solution of boron-doped diamond particles in water (the entire sample is dispersed, no coarse residue remains). This dispersion was further fractionated by centrifugation to give three size fractions containing nanodiamonds of different diameter (Figure 2, i–iii) with about 20% of the particles being below 70 nm and 35% of the particles being below 100 nm. The Raman spectra of the material after oxidation (Figure 1b, i–iii) show the removal of most of the disordered carbon and a distinct diamond peak as well as the Fano resonances. Furthermore, the oxidation leads to an oxidized diamond surface carrying carboxylic acid groups and other oxygen-containing surface groups. The zeta potential of the particles ( $-50\text{ mV}$  at pH 5.8 for fraction i,  $-44\text{ mV}$  at pH 5.3 for fraction ii, and  $-37\text{ mV}$  at pH 5.4 for fraction iii) is evidence of this process. The difference in absolute values can be attributed to the different particle size and the different amount of nondiamond carbon in the different size fractions. The finding of oxygenated surface groups is corroborated using IR spectroscopy by the occurrence of signals related to different types of carbonyl groups (Figure 3), whereas the varying degree of nondiamond carbon contamination can be seen in

the Raman spectra i–iii in Figure 1. Assuming a more or less truncated octahedral shape of the crystallites and taking the median of the particle size distribution into account, one can estimate specific surface areas of about 42, 21, and  $7 \text{ m}^2 \text{ g}^{-1}$  for the three size fractions of the boron-doped diamond nanoparticles.

These surface groups support the formation of stable colloidal solutions due to Coulomb stabilization of the nanoparticles. The colloidal solutions exhibit a

bright blue color as a result of the absorption properties of the boron centers in the diamond lattice and are stable for prolonged periods of time. With the particle sizes of the different fractions ranging from 45 to 100 to 300 nm (maxima of the individual size distributions), an efficient method for the production and colloidal dispersion of such boron-doped diamond nanoparticles has been found (Figure 2).

As diamond is a hard but rather brittle material, it can be cleaved. This cleavage occurs preferentially along low surface energy planes, like the {111} planes.<sup>34</sup> As can be seen from the HRTEM images (Figure 4), the resulting material after the milling and purification process still exhibits some degree of faceting, induced by the crushing. The first step in the milling process is the separation of the individual microcrystalline grains as well as smaller, overgrown nuclei at the basis of the substrate-free diamond films. The required amount of milling energy in this step is not very high, as mainly non-sp<sup>3</sup> bonds and noncovalent interactions in the grain boundaries have to be overcome. As discussed above, this initial crushing also liberates nondiamond carbon from the grain boundaries. In the subsequent “nanomilling” step, the microcrystallites themselves need to be cleaved. As this cleaving will preferentially occur along the weakest planes, a major issue with doped diamond crystallites is the location of the lattice defects. Some of us reported recently that the carbon

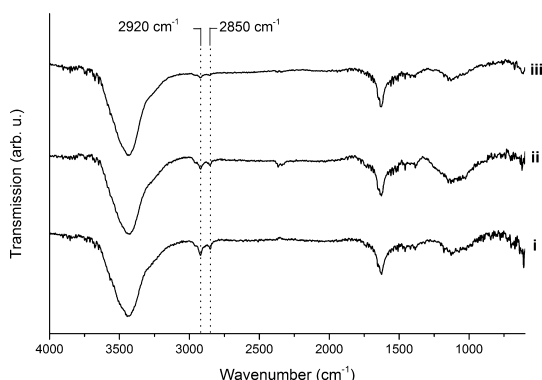


**Figure 3.** FTIR spectra of the three size fractions (i, ii, and iii; see Figure 2 for assignment) of diamond particles after production and purification. Besides the presence of surface water (and most likely surface OH groups) the IR reveals the existence of other oxygen-containing groups such as carbonyl and ether functions. Furthermore, the CH bonds at the surface result in additional bands around  $3000 \text{ cm}^{-1}$ .

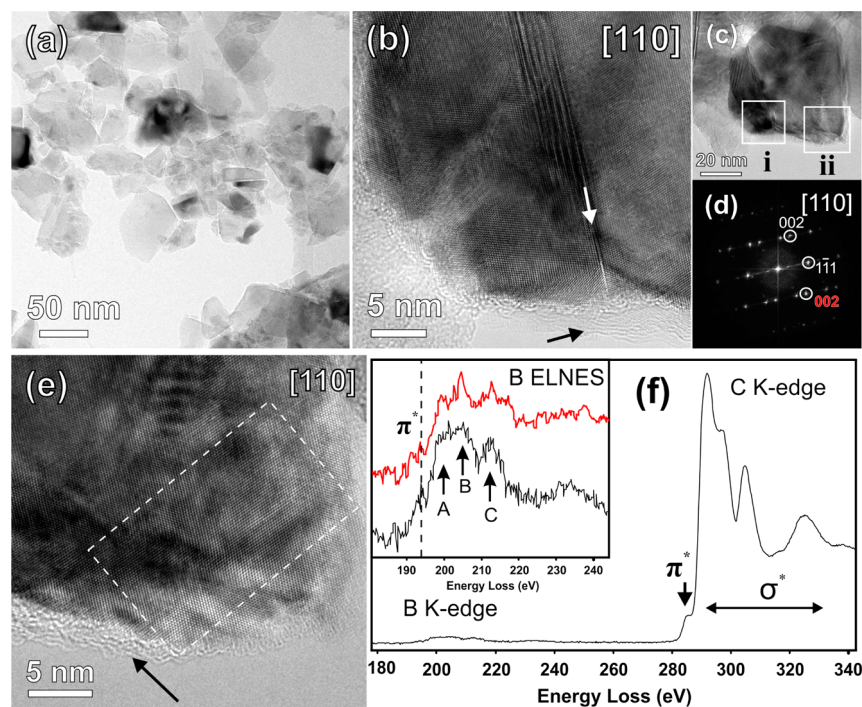


**Figure 4.** TEM imaging and EELS spectroscopy of the B:NDs. (a) Low-magnification TEM image showing the diamond particles have sizes ranging from  $\sim 30$  to  $70 \text{ nm}$  in diameter. (b and e) HRTEM images recorded from selected areas i and ii of a single diamond grain in c. (d) Fourier transform of the defect indicated by a white arrow in b, evidencing it is a  $\sqrt{3} \{111\}$  twin boundary. Both HRTEM images show amorphous and graphitic carbon covering the diamond particle surface (indicated by black arrows). (f) EELS spectrum acquired from a pristine diamond region (indicated by the white dashed rectangle in e), demonstrating the presence of boron. Inset black spectrum: B K-edge fine structure. Inset red spectrum: B K-edge fine structure reference for B tetrahedrally embedded in CVD diamond.

bond length at defective regions in a CVD diamond grain is longer ( $\sim 5$  pm bond elongation) than the classical C–C bond in diamond.<sup>35</sup> On top of this, the boron content is larger at defect-rich regions in the diamond lattice.<sup>36</sup> Crushing along lattice planes containing defect centers and along highly defective regions should be preferred over crushing along defect-free zones. As a consequence, boron centers will show up at the surface of the resulting particles, where they are not stabilized by the surrounding diamond lattice. It is known that defects near the diamond surface diffuse away.<sup>37</sup> As a result of this process, one should expect a decrease in boron content in the crushed material and indeed the initial concentration of about  $3 \times 10^{21} \text{ cm}^{-3}$  ( $\sim 17\,000 \text{ ppm}$ ) is reduced to approximately 13 000 ppm in the final diamond nanoparticles.<sup>7</sup> Nevertheless, this value is still extremely high, and to the best of our knowledge no boron-doped diamond nanoparticles have been reported so far at all.

In order to study the morphology of the boron-doped nanodiamond and investigate the distribution of boron within individual diamond nanoparticles, the boron-doped nanoparticles were studied using a combination of high-resolution transmission electron microscopy (HRTEM) and spatially resolved electron energy-loss spectroscopy (STEM-EELS).

Figure 4a is an overview bright-field TEM image of the produced material. The nanodiamond particle size is relatively monodisperse with particles ranging from approximately 30 to 70 nm in diameter, in accordance with the particle size distribution from light scattering. No debris from the milling procedure was found in between the nanoparticles. An overview image of a single 40 nm diameter nanodiamond particle is shown in Figure 4c, with two details of the image presented in Figure 4b and e. Even though the particles have been milled down to the nanoscale, individual particles can still contain defects, such as the  $\Sigma = 3 \{111\}$  twin boundary indicated by the white arrow in Figure 4b. The nature of the  $\Sigma = 3$  twin is evidenced through the Fourier transform of the HRTEM image, displayed in Figure 4d. The surface of the nanoparticle is covered by a nondiamond carbon shell, with a thickness of 3–5 nm (see example regions indicated by black arrows in Figure 4b and e). As all TEM experiments were carried out at a relatively low acceleration voltage of 120 kV, the observed shell, which was stable during the TEM measurements, is not formed by exposure to the electron beam, but is the result of the high mechanical impact during the milling.<sup>38</sup>

The presence of boron incorporated into the individual nanoparticles is evidenced by electron energy-loss spectroscopy. An EELS spectrum, acquired from the region indicated by the white rectangle in Figure 4e, is plotted in Figure 4f. The presence of boron

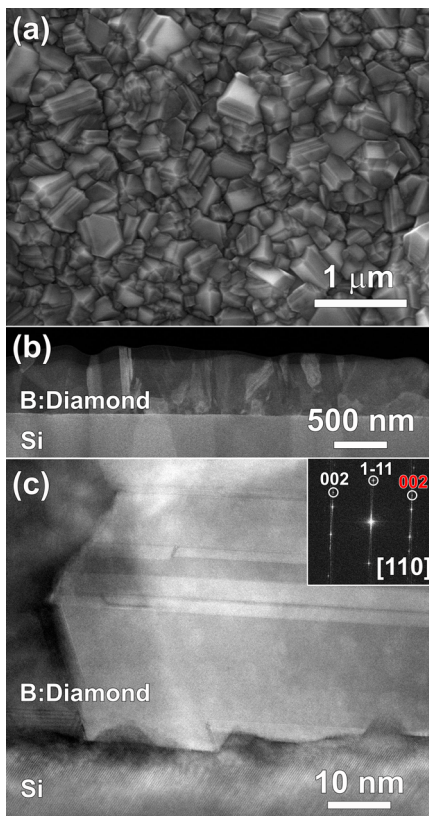


**Figure 5.** B:NCD film grown on B:nanodiamond seeds. (a) SEM image of a B:NCD film, grown on a Si substrate. (b) Cross-sectional ADF-STEM image of the B:NCD film on Si. (c) High-resolution ADF-STEM image of the interface between the Si substrate and the B:NCD film. The high-quality B: diamond (evidenced by the inset Fourier transform pattern) grows directly on top of the Si, without the presence of any nondiamond phases at the interface.

is evidenced through the B K-edge at 190 eV. Using standard EELS quantification techniques, the boron content was determined to be  $1.3 \pm 0.2 \text{ at. \%}$  ( $\sim 13\,000 \text{ ppm} \approx 2.3 \times 10^{21} \text{ cm}^{-3}$ ). This concentration is somewhat below the boron concentration determined for the B-doped microcrystalline diamond film prior to the nanoparticle formation. This loss of boron has its origin in the breaking down of grain boundaries and defective regions in the material during milling, where B is known to be enriched, as discussed above.

The fine structure of the carbon K-edge, starting at 285 eV, mainly shows features associated with  $\text{sp}^3$ -hybridized carbon in diamond ( $\sigma^*$  contribution). The small  $\pi^*$  contribution at 285 eV arises from the graphitic material at the nanoparticle surface. The coordination of B in the nanoparticles can be determined through investigation of the energy-loss near-edge structure (ELNES) of the boron K-edge. The ELNES signature is known to be sensitive to the local environment of the probed atomic species. In the inset in Figure 4f, the fine structure of the B K-edge (in black) is plotted together with a reference spectrum for

tetrahedrally incorporated B in diamond (in red).<sup>39</sup> The three peaks A, B, and C, which are present in both spectra, are indicative of tetrahedrally embedded boron in diamond and, therefore, indicate that most of the B is embedded in the diamond lattice. The small  $\pi^*$  contribution in the B fine structure most likely arises from B embedded in a planar configuration in the nondiamond carbon surface shell or at defects in the material, but might also originate from heavily distorted tetrahedral B sites.

One of the most technologically relevant applications of the synthesized boron-doped nanodiamonds is the use as seeds for the growth of B:NCD films. In many applications of B:NCD films, it is of great importance that the full film is conductive and, therefore, doped with boron. When nondoped seeds are used (which is usually the case at this point in time), this leads to nonconductive regions in between the substrate and the B:NCD film, which is particularly unfavorable for B:NCD films of a few tens to hundreds of nanometers in thickness. To test the applicability of our B:diamonds to the seeding, we grew a B:NCD film on a Si substrate, with B:nanodiamonds providing the seed crystallites for CVD.<sup>40</sup>

A SEM image of the grown film, presented in Figure 5a, shows a dense film growth. This same dense growth is evidenced by a cross-sectional annular dark-field (ADF-)STEM image, presented in Figure 5b. It is clear from the image that the polycrystalline B:diamond film has a film thickness of approximately 600 nm and is grown directly on top of the Si substrate. The high-resolution ADF-STEM image in Figure 5c evidences that the B:NCD grains are of high crystalline quality, with minimal nondiamond carbon at the grain interfaces. The diamond grains show the presence of typical  $\Sigma = 3 \{111\}$  twin boundaries. Importantly, the

B:diamond has grown directly on the Si film, without any other insulating phases present at the interface.

## CONCLUSION

In summary, we have produced intrinsically boron-doped diamond nanoparticles for the first time. The starting material of polycrystalline CVD diamond film with a boron content of  $\sim 17\,000$  ppm was subjected to a multistep milling procedure, leading to diamond nanoparticles with a crystallite size of 30–70 nm. The boron content of these particles was measured at  $\sim 13\,000$  ppm, indicating that the lattice defects were not destroyed during the mechanical treatment. A multistep acid treatment led to the removal of surface-bound  $sp^2$  carbon as well as the removal of most of the disordered carbon from the surface of the resulting particles. A stable, bright blue colored colloidal of the boron-doped diamond nanoparticles was obtained. The detailed HRTEM and EELS analysis showed the presence of boron atoms at the C-lattice positions as well as the tetragonal coordination of these dopants. The diamond lattice did not suffer substantial damage in the applied treatment. The process relies on the production of suitably doped diamond films and requires rather harsh crushing and cleaning conditions. Nevertheless, it yields diamond nanoparticles with high boron content distributed over the whole particle. We demonstrated the use of these samples as seeding for the growth of boron-doped CVD diamond that does not have an insulating layer between the substrate and the film. In the future we will use these boron-doped diamond nanoparticles for a variety of applications, *e.g.*, electrochemistry, thermal management, seeding applications, and the study of fundamental properties of boron-doped diamond nanoparticles such as superconductivity.

## METHODS

**Equipment.** The following equipment was used. CVD growth: ASTeX 6500 series MWPECVD reactor (Seki Diamond Systems, Japan). Ball mill: PULVERISETTE 23 (Fritsch, Germany) equipped with grinding bowl and balls (3 mm) made from tempered steel. Dynamic light scattering and zeta potential: Zetasizer Nano (Malvern, UK). Raman spectra: DXR Raman microscope (Thermo, UK). SEM: Ultra Plus field emission scanning electron microscope equipped with a GEMINI e-Beam column operated at 1.00 kV (Zeiss, Germany). HRTEM: FEI Titan 80-300.

**Growth of Diamond Film.** (a) Boron-doped film for nanoparticle production: A cleaned, double-sided polished silicon wafer (2 in.) was dip-coated in a water-based state-of-the-art colloidal suspension of ultradispersed nanodiamonds for seeding and subsequently spin-dried.<sup>36</sup> The suspension contained 6–7 nm sized detonation nanodiamonds from NanoCarbon Institute Co., Ltd., and featured a zeta potential of  $45 \pm 5$  mV.

After seeding, a  $14.5 \mu\text{m}$  thick microcrystalline film was deposited in an ASTeX 6500 series MW PE CVD reactor at 3% C/H ratio and 5000 ppm B/C ratio. The B-containing feed-gas was trimethylborane (TMB). Throughout the growth process the plasma power was maintained at 4000 W, the working pressure was kept at 45 Torr (6666.1 Pa), while the total gas flow was

500 sccm. These conditions resulted in an initial deposition temperature of 750 °C, which further decreased to 700 °C during the growth.

In order to obtain free-standing diamond, the Si substrate was entirely etched in an aqueous 25% tetramethylammonium hydroxide solution at around 80 °C for several hours.

(b) Boron-doped film using the B:DNPAs as seeds: The B:nanodiamond colloid was drop-casted on a cleaned  $1 \times 1 \text{ cm}^2$  Si substrate and slowly rotated while gently blow-dried. The B:NCD film deposited during 4 h in the previously mentioned reactor in 1% C/H with 5000 ppm B/C in the gas phase. The CVD plasma was operated at 3500 W, 35 Torr (4666.3 Pa), and a total gas flow of 500 sccm, which resulted in a substrate temperature of 800 °C.

**Production of Diamond Nanoparticles.** A 174 mg amount of the boron-doped diamond wafer and 4 mL of 2-propanol were placed in a 10 mL grinding bowl (tempered steel) of a PULVERISETTE 23 vibration mill (Fritsch, Idar-Oberstein) with 20 grinding balls (tempered steel,  $d = 3$  mm). The sample was treated 8 h (4 cycles of 2 h) in the mill at a frequency of  $50 \text{ s}^{-1}$ . After cooling to room temperature the resulting powder was flushed out of the beaker with 30 mL of water. To remove iron abrasion, 30 mL of concentrated hydrochloric acid was added to the suspension

in a 100 mL round-bottom flask, equipped with a magnetic stirring bar and a condenser. The mixture was stirred at 125 °C (bath temperature) for 16 h. After cooling to room temperature, 30 mL of water was added and the diamond was centrifuged. The acids were removed by several washing/centrifugation cycles (15 min, 15,000 rpm, 25150g) using doubly distilled water until pH 5.6 was reached. During the purification process, the stable supernatant was collected, submitted to fractionated centrifugation for particle size separation, and dialyzed for 4 days (cellulose hydrate dialysis tube, cutoff 10–20 kDa, MICRODIN-NADIR) with doubly distilled water. By 30 min centrifugation at 40,000 rpm (163000g), very small particles of 8–27 nm could be collected. As Raman spectroscopy revealed only the G- and D-bands of amorphous and graphitic carbon, these had to be removed by treatment with a mixture of concentrated sulfuric and nitric acid. The carbon colloid was destabilized by addition of a few drops of sulfuric acid and centrifuged 15 min at 40,000 rpm (163000g). The brown solid was dispersed in a mixture of 20 mL of concentrated sulfuric acid and 2 mL of concentrated nitric acid. The mixture was stirred at 180 °C (bath temperature) for 16 h. The colloid became colorless, and no solid could be isolated.

Since in the precipitate of the centrifugations diamond was detectable with Raman spectroscopy, the milling process was repeated. After the removal of the iron abrasion with concentrated hydrochloric acid as described, the oxidation was carried out using a 9:1 mixture of concentrated sulfuric acid and concentrated nitric acid. The aqueous workup was carried out as described by cycles of washing and centrifugation with doubly distilled water. Up to pH 5.8, no stable supernatant could be received by 15 min centrifugation at 15,000 rpm (25150g), so the centrifugation speed and time were reduced to 5 min and 5000 rpm (2790g). Now a clear, deep blue colloid with particle sizes of 45 to 143 nm could be isolated. By increasing the centrifugation speed to 8000 rpm (7150g), the bigger particles were removed and the resulting particle sizes, measured by DLS, were reduced to 25–100 nm. In total, three size fractions of ~25–100, 40–400, and 30–1000 nm have been obtained. TEM images and Raman measurement showed that the collected particles were indeed diamond containing boron doping.

**High-Resolution TEM Imaging and Electron Energy-Loss Spectroscopy.** A TEM sample of the material was prepared by placing a few drops of a liquid dispersion of the B:NDs on a holey carbon film coated on a copper mesh TEM grid. All electron microscopy and spectroscopy experiments were carried out on a FEI Titan 80-300 “cubed” microscope, fitted with an aberration-corrector for the imaging lens and the probe-forming lens. The microscope was operated at 120 kV, in order to minimize knock-on damage to the diamond particles. EELS experiments were performed in STEM mode using a convergence angle  $\alpha$  of ~22 mrad and a collection semiangle  $\beta$  of ~17 mrad. The spectra were acquired at an energy dispersion of 0.25 eV/pixel and an energy resolution of approximately 1.5 eV. Quantification of the B concentration was performed in the Digital Micrograph software package. The ADF-STEM experiments shown in Figure 5 were performed on the same Titan “cubed” microscope, operated at 300 kV. The convergence semiangle  $\alpha$  was 22 mrad, and the collection semiangle for ADF imaging was 20 mrad. The cross-sectional lamella was prepared by a focused ion beam lift-out procedure, carried out in a FEI Helios FIB-SEM.

**Conflict of Interest:** The authors declare no competing financial interest.

**Supporting Information Available:** Raman spectra, DRIFT data, photograph of nondiamond colloid. This material is available free of charge via the Internet at <http://pubs.acs.org>.

**Acknowledgment.** We gratefully acknowledge funding from the Deutsche Forschungsgemeinschaft DFG (FOR1493 and contract KR3316/3-1), the Fonds der Chemischen Industrie, the Research Foundation Flanders (FWO-Vlaanderen) (G.0555.10N, G.0568.10N, G.0456.12, G.0044.13N and a postdoctoral scholarship for S.T.), the EU FP7 through Marie Curie ITN “MATCON” (PITN-GA-127 2009-238201), the Collaborative Project “DINAMO” (No. 245122), and a contract for an Integrated Infrastructure Initiative, Reference No. 312483-ESTEEM2.

## REFERENCES AND NOTES

- Gaillou, E.; Wang, W.; Post, J. E.; King, J. M.; Butler, J. E.; Collins, A. T.; Moses, T. M. The Wittelsbach-Graff and Hope Diamonds: Not Cut from the Same Rough. *Gems Gemol.* **2010**, *46*, 80–88.
- Gaillou, E.; Post, J. E.; Butler, J. E. Boron in Natural Type IIb Blue Diamonds: Chemical and Spectroscopic Measurements. *Am. Mineral.* **2012**, *97*, 1–18.
- Kim, D. Y.; Yang, J. C.; Kim, H. W.; Swain, G. M. Heterogeneous Electron-Transfer Rate Constants for Ferrocene and Ferrocene Carboxylic Acid at Boron-Doped Diamond Electrodes in a Room Temperature Ionic Liquid. *Electrochim. Acta* **2013**, *94*, 49–56.
- Channon, R. B.; Newland, J. C.; Bristow, A. W. T.; Ray, A. D.; Macpherson, J. V. Selective Detection of Hydrazine in the Presence of Excess Electrochemically Active Pharmaceutical Ingredients Using Boron Doped Diamond Metal Nanoparticle Functionalised Electrodes. *Electroanalysis* **2013**, *25*, 2613–2619.
- Kato, H.; Hees, J.; Hoffmann, R.; Wolfer, M.; Yang, N.; Yamasaki, S.; Nebel, C. E. Diamond Foam Electrodes for Electrochemical Applications. *Electrochim. Commun.* **2013**, *33*, 88–91.
- Zhang, G.; Janssens, S. D.; Vanacken, J.; Timmermans, M.; Vacik, J.; Atakli, G. W.; Decelle, W.; Gillijns, W.; Goderis, B.; Haenen, K.; et al. Role of Grain Size in Superconducting Boron-Doped Nanocrystalline Diamond Thin Films Grown by CVD. *Phys. Rev. B* **2011**, *84*, 214517.
- Janssens, S. D.; Pobedinskas, P.; Vacik, J.; Petrakova, V.; Rutten, B.; D’Haen, J.; Nesladek, M.; Haenen, K.; Wagner, P. Separation of Intra- and Intergranular Magnetotransport Properties in Nanocrystalline Diamond Films on the Metallic Side of the Metal-Insulator Transition. *New J. Phys.* **2011**, *13*, 083008.
- Zhang, G.; Turner, S.; Ekimov, E. A.; Vanacken, J.; Timmermans, M.; Samuely, T.; Sidorov, V. A.; Stishov, S. M.; Lu, Y.; Deloof, B.; et al. Global and Local Superconductivity in Boron-Doped Granular Diamond. *Adv. Mater.* **2014**, *26*, 2034–2040.
- Kummer, K.; Fondacaro, A.; Yakhou-Harris, F.; Sessi, V.; Pobedinskas, P.; Janssens, S. D.; Haenen, K.; Williams, O. A.; Hees, J.; Brookes, N. B. Thin Conductive Diamond Films as Beam Intensity Monitors for Soft X-Ray Beamlines. *Rev. Sci. Instrum.* **2013**, *84*, 035105.
- Ay, A.; Swope, V. M.; Swain, G. M. The Physicochemical and Electrochemical Properties of 100 and 500 nm Diameter Diamond Powders Coated with Boron-Doped Nanocrystalline Diamond. *J. Electrochem. Soc.* **2008**, *155*, B1013–B1022.
- Guoa, L.; Swopea, V. M.; Merzougui, B.; Protsailob, L.; Shaob, M.; Yuana, Q.; Swain, G. M. Oxidation Resistance of Bare and Pt-Coated Electrically Conducting Diamond Powder as Assessed by Thermogravimetric Analysis. *J. Electrochem. Soc.* **2010**, *157*, A19–A25.
- Spätaru, N.; Zhang, X.; Spätaru, T.; Tryk, D. A.; Fujishima, A. Platinum Electrodeposition on Conductive Diamond Powder and Its Application to Methanol Oxidation in Acidic Media. *J. Electrochem. Soc.* **2008**, *155*, B264–B269.
- Kim, D.; Merzougui, Y. B.; Swain, G. M. Preparation and Characterization of Glassy Carbon Powder Modified with a Thin Layer of Boron-Doped Ultrananocrystalline Diamond (B-UNCD). *Chem. Mater.* **2009**, *21*, 2705–2713.
- Ukrainstev, E.; Kromka, A.; Janssen, W.; Haenen, K.; Rezek, B. Bonding of Polypyrrole to Boron Doped Diamond by Surface Termination. *Int. J. Electrochem. Sci.* **2013**, *8*, 17–26.
- Tsigkourakos, M.; Hantschel, T.; Arstila, K.; Vandervorst, W. Diamond Nano-particle Seeding for Tip Moulding Application. *Diamond Relat. Mater.* **2013**, *35*, 14–18.
- Doherty, M. W.; Manson, N. B.; Delaney, P.; Jelezko, F.; Wrachtrup, J.; Hollenberg, L. C. L. The Nitrogen-Vacancy Colour Centre in Diamond. *Phys. Rep.* **2013**, *528*, 1–45.
- Neu, E.; Arend, C.; Gross, E.; Guldner, F.; Hepp, C.; Steinmetz, D.; Zschergel, E.; Ghodbane, S.; Sternschulte, H.; Steinmüller-Nethl, D.; et al. Narrowband Fluorescent Nanodiamonds Produced from Chemical Vapor Deposition Films. *Appl. Phys. Lett.* **2011**, *98*, 243107.

18. Aharonovich, I.; Castelletto, S.; Simpson, D. A.; Su, C.-H.; Greentree, A. D.; Prawer, S. Diamond-Based Single-Photon Emitters. *Rep. Prog. Phys.* **2011**, *74*, 076501.
19. Vlasov, I. I.; Shiryayev, A. A.; Rendler, T.; Steinert, S.; Lee, S.-Y.; Antonov, D.; Voeroes, M.; Jelezko, F.; Fisenko, A. V.; Semjonova, L. F.; et al. Molecular-Sized Fluorescent Nanodiamonds. *Nat. Nanotechnol.* **2014**, *9*, 54–58.
20. Balasubramanian, G.; Chan, I. Y.; Kolesov, R.; Al-Hmoud, M.; Tisler, J.; Shin, C.; Kim, C.; Wojcik, A.; Hemmer, P. R.; Krueger, A.; et al. Nanoscale Imaging Magnetometry with Diamond Spins under Ambient Conditions. *Nature* **2008**, *455*, 648–651.
21. Arroyo-Camejo, S.; Adam, M.-P.; Besbes, M.; Hugonin, J.-P.; Jacques, V.; Greffet, J.-J.; Roch, J.-F.; Hell, S. W.; Treussart, F. Stimulated Emission Depletion Microscopy Resolves Individual Nitrogen Vacancy Centers in Diamond Nanocrystals. *ACS Nano* **2013**, *7*, 10912–10919.
22. Bayn, I.; Bolker, A.; Cytermann, C.; Meyler, B.; Richter, V.; Salzman, J.; Kalish, R. Diamond Processing by Focused Ion Beam-Surface Damage and Recovery. *Appl. Phys. Lett.* **2011**, *99*, 183109.
23. Bosia, F.; Argiolas, N.; Bazzan, M.; Fairchild, B. A.; Greentree, A. D.; Lau, D. W. M.; Olivero, P.; Picollo, F.; Rubanov, S.; Prawer, S. Direct Measurement and Modelling of Internal Strains in Ion-Implanted Diamond. *J. Phys.: Condens. Matter* **2013**, *25*, 385403.
24. Hausmann, B. J. M.; Babinec, T. M.; Choy, J. T.; Hodges, J. S.; Hong, S.; Bulu, I.; Yacoby, A.; Lukin, M. D.; Loncar, M. Single-Color Centers Implanted in Diamond Nanostructures. *New J. Phys.* **2011**, *13*, 045004.
25. Chakraborty, R.; Sharma, S. C.; LaRoque, J. K. A Study of the Structural and Vibrational Properties of Diamond Nanoparticles Grown by Chemical Vapor Deposition. *J. Nano Res.* **2010**, *12*, 123–130.
26. Vul', A. Ya.; Golubev, V. G.; Grudinkin, S. A.; Krüger, A.; Naramoto, H. Diamond Films: Initial CVD Growth Stage Using Nanodiamonds as Nucleation Centers. *Techn. Phys. Lett.* **2002**, *28*, 787–789.
27. Stacey, A.; Aharonovich, I.; Prawer, S.; Butler, J. E. Controlled Synthesis of High Quality Micro/Nano-Diamonds by Microwave Plasma Chemical Vapor Deposition. *Diamond Relat. Mater.* **2009**, *18*, 51–55.
28. Neu, E.; Guldner, F.; Arend, C.; Liang, Y.; Ghodbane, S.; Sternschulte, H.; Steinmüller-Nethl, D.; Krueger, A.; Becher, C. Low Temperature Investigations and Surface Treatments of Colloidal Narrowband Fluorescent Nanodiamonds. *J. Appl. Phys.* **2013**, *113*, 203507.
29. Boudou, J.-P.; Tisler, J.; Reuter, R.; Thorel, A.; Curmi, P. A.; Jelezko, F.; Wrachtrup, J. Fluorescent Nanodiamonds Derived from HPHT with a Size of Less Than 10 nm. *Diamond Relat. Mater.* **2013**, *37*, 80–86.
30. Pruvost, F.; Deneuville, A. Analysis of the Fano in Diamond. *Diamond Relat. Mater.* **2001**, *10*, 531–535.
31. Krüger, A.; Ozawa, M.; Kataoka, F.; Fujino, T.; Suzuki, Y.; Aleksenskii, A. E.; Vul', A. Ya.; Osawa, E. Unusually Tight Aggregation in Detonation Diamond: Identification and Disintegration. *Carbon* **2005**, *43*, 1722–1730.
32. Liang, Y.; Ozawa, M.; Krueger, A. A General Procedure to Functionalise Agglomerating Nanoparticles Demonstrated on Nanodiamond. *ACS Nano* **2009**, *3*, 2288–2296.
33. Kuznetsov, V. L.; Aleksandrov, M. N.; Zagoruiko, I. V.; Chuvilin, A. L.; Moroz, E. M.; Kolomiichuk, V. N.; Likholobov, V. A.; Brylyakov, P. M.; Sakovich, G. V. Study of Ultradispersed Diamond Powders Obtained Using Explosion Energy. *Carbon* **1991**, *29*, 665–668.
34. Telling, R. H.; Pickard, C. J.; Payne, M. C.; Field, J. E. Theoretical Strength and Cleavage of Diamond. *Phys. Rev. Lett.* **2000**, *84*, 5160–5163.
35. Lu, Y.-G.; Turner, S.; Verbeeck, J.; Janssens, S. D.; Haenen, K.; Van Tendeloo, G. Local Bond Length Variations in Boron-Doped Nanocrystalline Diamond Measured by Spatially Resolved Electron Energy-Loss Spectroscopy. *Appl. Phys. Lett.* **2013**, *103*, 032105.
36. Lu, Y.-G.; Turner, S.; Verbeeck, J.; Janssens, S. D.; Wagner, P.; Haenen, K.; Van Tendeloo, G. Direct Visualization of Boron Dopant Distribution and Coordination in Individual Chemical Vapor Deposition Nanocrystalline B-Doped Diamond Grains. *Appl. Phys. Lett.* **2012**, *101*, 041907.
37. Barnard, A. S.; Russo, S. P.; Snook, I. K. Simulation and Bonding of Dopants in Nanocrystalline Diamond. *J. Nanosci. Nanotechnol.* **2005**, *5*, 1395–1407.
38. Turner, S.; Shenderova, O.; Da Pieve, F.; Lu, Y.-G.; Yücelen, E.; Verbeeck, J.; Lamoen, D.; Van Tendeloo, G. Aberration-Corrected Microscopy and Spectroscopy Analysis of Pristine, Nitrogen Containing Detonation Nanodiamond. *Phys. Status Solidi A* **2013**, *210*, 1976–1984.
39. Turner, S.; Lu, Y.-G.; Janssens, S. D.; Da Pieve, F.; Lamoen, D.; Verbeeck, J.; Haenen, K.; Wagner, P.; Van Tendeloo, G. Local Boron Environment in B-Doped Nanocrystalline Diamond. *Nanoscale* **2012**, *4*, 5960–5964.
40. Williams, O. A.; Douhéret, O.; Daenen, M.; Haenen, K.; Osawa, E.; Takahashi, M. Enhanced Diamond Nucleation on Monodispersed Nanocrystalline Diamond. *Chem. Phys. Lett.* **2007**, *445*, 255–258.